FISEVIER

Contents lists available at ScienceDirect

Additive Manufacturing Letters

journal homepage: www.elsevier.com/locate/addlet



Short Communication



High through-thickness thermal conductivity of 3D-printed composites via rotational direct ink writing

Jackson K. Wilt^a, Nadim S. Hmeidat^a, John W. Bohling^a, Brett G. Compton^{a,b,*}

- ^a Mechanical. Aerospace, and Biomedical Engineering Department. University of Tennessee, Knoxville, TN 37996. USA
- ^b Materials Science and Engineering Department, University of Tennessee, Knoxville, TN 37996, USA

ARTICLE INFO

Keywords: Additive manufacturing Composites Thermal conductivity 3D printing Rotational direct ink writing Fiber orientation Epoxy Carbon fiber

ABSTRACT

Composites printed using material extrusion additive manufacturing (AM) typically exhibit alignment of highaspect-ratio reinforcements parallel to the print direction. This alignment leads to highly anisotropic stiffness, strength, and transport properties. In many cases, it would be desirable to increase mechanical and transport properties transverse to the print direction, for example, in 3D-printed heat sinks or heat exchangers where heat must be moved efficiently between printed roads or layers. Rotational direct ink writing (RDIW), where the deposition nozzle simultaneously rotates and translates during deposition, provides a method to reorient fibers transverse to the print direction during the printing process. In the present work, carbon fiber-reinforced epoxy composites were printed by RDIW with a range of nozzle rotation rates and the in-plane and through-thickness thermal conductivity was measured. In addition, the orientation of carbon fiber (CF) in the composites was measured using optical microscopy and image analysis, from which second-order fiber orientation tensors were calculated. These results showed that the orientation of CF became less anisotropic as nozzle rotation rate increased, leading to increased through-thickness thermal conductivity, which increased by 40% at the highest rotation rate. The orientation tensors also showed that RDIW was more effective at reorienting fibers within the in-plane transverse direction compared to the through-thickness transverse direction. The results presented here demonstrate that a current weakness of material extrusion AM composites-poor thermal conductivity in the through-thickness direction—can be significantly improved with RDIW.

1. Introduction

Material extrusion additive manufacturing (AM) fabricates 3D objects by selectively extruding material in a layer-by-layer sequence [1] and includes both Fused Filament Fabrication (FFF) and Direct Ink Writing (DIW). Frequently, these techniques utilize high-aspect-ratio filler materials, such as short fibers [2–5], nanotubes [6,7], and nanoplatelets [8], to create 3D-printed composites with high strength and stiffness. DIW inks are typically shear thinning and display a yield stress that allows the printed form maintain shape after printing [8]. Fibers impart shear thinning to suspensions but also lead to clogging if loading is too high, therefore composite inks are usually designed to contain up to $\sim\!15$ vol.% short fibers in addition to another viscosifying filler that more effectively imparts yield strength [9]. During extrusion, filler materials with high aspect ratios are oriented predominantly parallel to the print direction due to shear stresses within the carrier resin [3–5,10,

11]. This orientation leads to anisotropy in mechanical and transport properties, which can be used to great effect if print paths are optimized for fiber orientation for a given load case [12–15]. However, with conventional material extrusion technologies, filler orientation in printed composites is still limited to directions within the layer plane. That is, although in-plane anisotropy can be optimized or mitigated through choice of print path, few tools exist to orient fibers in the through-thickness direction in order to improve strength, stiffness, or transport properties transverse to the layer plane. Such capabilities could increase the viability of using material extrusion AM in applications such as 3D-printed heat sinks or heat exchangers, which have been investigated by several groups [16–20].

Some promising efforts at controlling filler orientation for AM have been made, including magnetic fields [21,22], electrical fields [23,24], ultrasonic vibration [25–27], and oscillation [11]. These methods were used *in-situ* or post-extrusion to reorient the printed fillers. However,

E-mail address: bcompto1@utk.edu (B.G. Compton).

^{*} Corresponding author at: University of Tennessee, Mechanical, Aerospace, and Biomedical Engineering Department, 1512 Middle Drive 201 Dougherty Engineering Building Knoxville, TN 37996, USA.

these methods have some limitations. For instance, magnetic or electrical fields can only impose reorientation forces on electromagnetically responsive fillers, such as carbon or metallic particles. The methods based on ultrasonic vibration or oscillation are viable with non-conductive fillers, but the resulting mechanical disturbance of roads during deposition can potentially affect the structural integrity of the print prior to curing. Although promising, these approaches highlight the need for a reorientation technique that is material-agnostic and amenable to material extrusion AM.

Raney and Compton et al. developed a DIW method with a rotational print head, referred to as rotational direct ink writing (RDIW) [28]. In RDIW, the printing apparatus is outfitted with a drive-motor for programmable rotation of the nozzle (Fig. 1(a)) during printing. Unlike conventional DIW, where fibers tend to align along the print direction (Fig. 1(b)), a rotating nozzle imposes an additional shear field between the moving nozzle and the stationary substrate that effectively reorients fibers or fillers into a helical arrangement (Fig. 1(c)). The theoretical helical angle with respect to the road axis is given as $\varphi = tan^{-1}(\overline{\omega})$, where $\overline{\omega} = \frac{R\omega}{\nu}$ is the dimensionless rotation rate, ν is the translation rate of the print head (i.e. the print speed), ω is the nozzle rotation rate, and R is the radius of the nozzle outlet.

Raney and Compton et al. demonstrated that RDIW effectively modified the orientation of nonmagnetic, high-aspect-ratio fillers like carbon fibers (CFs), and that their reorientation during printing enabled spatial control over elastic stiffness and improved damage tolerance in printed epoxy-CF composites. More recently, Raney and colleagues have used RDIW to control orientation of milled glass fibers in silicone composites [29], demonstrating improved toughness and stiffness of the base silicone, while Larson et al. [30] recently expanded RDIW to include multiple material streams embedded in the single extruded road. Using stiff and compliant UV-curable acrylic, they also demonstrated that RDIW can be used to control elastic properties and improve toughness compared to conventionally-printed materials.

Beside structural properties, RDIW offers promise for spatially-tailoring electrical, optical, and thermal properties as well. Some work has characterized thermal conductivity in 3D-printed composites. For example, Spoerk et al. showed that material extrusion AM results in strong anisotropy in the thermal conductivity of printed polypropylene-CF composites [31]. However, despite recent advances, the effects of RDIW on thermal conductivity in printed composites have not yet been investigated. Here, for the first time, we measure the in-plane and through-thickness thermal conductivity for RDIW-printed epoxy-CF composites and show that the through-thickness thermal conductivity can be improved up to 40% for this material system using RDIW. In addition, for the first time, fiber orientation tensors are calculated for the RDIW-printed composites and used to rationalize thermal

conductivity measurements.

2. Materials and methods

2.1. Materials and ink formulation

An epoxy-CF ink was formulated by mixing 5 g of dicyandiamide latent curing agent (Dicyanex 1400B, Evonik Industries AG, Essen, Germany) into 100 g of epoxy resin (Epon 826, Hexion Inc., Columbus, OH) using a centrifugal planetary SpeedMixer (FlackTek, Inc., Landrum, SC) at 1800 rpm for 2 min. Next, 15 g (7.9 vol.%; 11.4 wt.%) of chopped carbon fiber (AS4/BR102, Hexcel Co., Stamford, CT) was added and mixed for a total period of 12 min at 2000 rpm. The mixing period was divided into 3 min intervals, with each interval followed by a rest period of ~10 min to allow the mixture to cool. Although the fibers were added in the form of 6-mm-long chopped ribbons, these disperse and fracture during the mixing process, resulting in volume-averaged fiber length of \sim 300 μ m, based on extensive characterization of similar formulations by Hmeidat et al. [9] and Pierson et al. [32]. Next, 10 g (5.9 vol.%; 7.6 wt.%) of nanoclay (Garamite 7305, BYK Chemie GmbH, Wesel, Germany) was added in two steps. For each of the two steps, 5 g nanoclay was added and mixed at 2000 rpm for 3 min, followed by a rest period of ~10 min. Next, the batch was mixed for another 3 min period at 2000 rpm. Finally, 2 g of reactive diluent (EPODIL 748, Evonik Industries AG, Essen, Germany) was added to the final mixture and mixed at 2000 rpm for 2 min. All mixing steps were conducted under vacuum of 0.1 atm. Ink composition and properties of the constituents are summarized in Table 1.

2.2. Epoxy-CF composite fabrication by rotational direct ink writing

The RDIW printer is based on a 3-axis ShopBot CNC router (Shopbot Tools Inc., Durham, NC) fitted with a 10-cc syringe cartridge (Nordson EFD, Westlake, OH) mounted in a pneumatic pressure adapter (HP3, Nordson EFD, Westlake, OH). The pneumatic pressure adaptor provides a 4x increase in pressure applied to the syringe cartridge and is connected to the building air supply through a regulator to allow the user to set the driving pressure. An 872-µm-diameter, tapered Luer-lock syringe tip (McMaster-Carr, Elmhurst, IL) was used as the extrusion nozzle. To enable RDIW, a rotary union was located between the outlet of the syringe cartridge and the deposition nozzle (Fig. 1(a)) and the nozzle itself was mounted in a custom-made adaptor that was fitted in a bearing block to allow free rotation about the axis of the nozzle. A pulley was mounted to the nozzle adaptor. Rotation at prescribed rates was achieved through a stepper motor connected to the pulley by a timing belt, as shown in Fig. 1(a). The setup used here is substantially similar to that

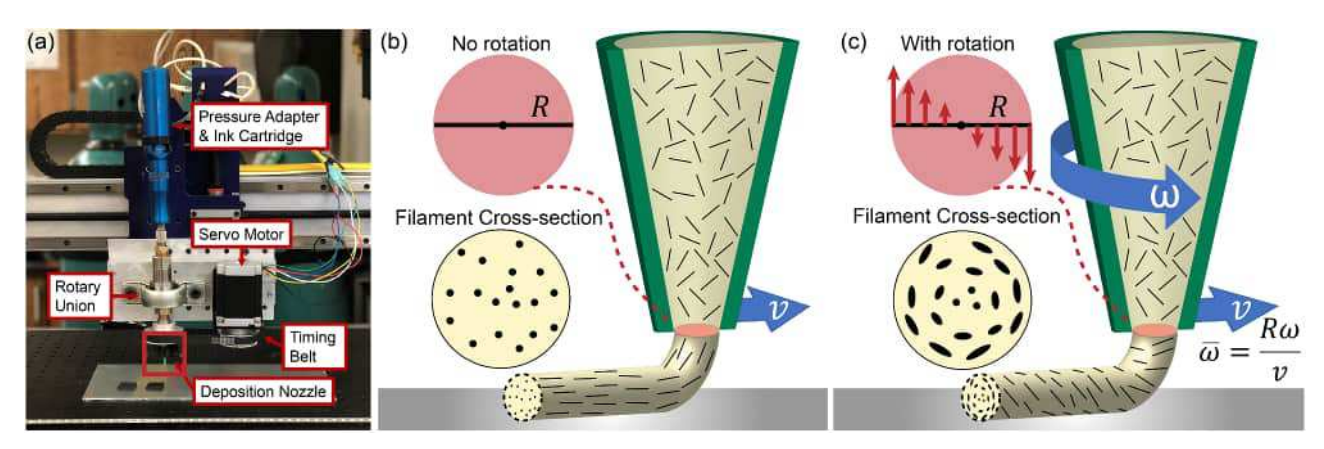


Fig. 1. (a) Photograph of the RDIW apparatus, showing the components pertaining to the nozzle rotation mechanism. Schematic illustrations showing (b) the normal orientation of fiber-like reinforcements in an extruded road and cross-section, and (c) the modified orientation and cross-section produced by RDIW. Note that RDIW produces greater fiber reorientation adjacent to the outer surface of the road compared to the center of the road.

Table 1Ink composition and constituent properties.

Constituent	Batch mass (g)	Weight%	Volume%	Initial form	Density (g/cm3)	Thermal conductivity (W/m.K)
Epon 826	100	75.7	80.8	Liquid	1.16	0.27*
Dicyanex 1400B	5	3.8	3.3	Powder	1.4	
Epodil 748	2	1.5	2.1	Liquid	0.89	
Garamite nanoclay	10	7.6	5.9	Aggregates of nanoparticles	1.6	
Hexcel carbon fibers	15	11.4	7.9	6-mm chopped ribbon, 7.1-µm diameter	1.79	6.83 [33]

^{*} Estimated based on a similar formulation presented in [6].

described in Raney and Compton et al. (2018) [28].

Open-source Scilab software [34] was used to generate g-code files for printing, and a unidirectional print path was chosen with the print path oriented along the x-axis of the printer. Five pairs of samples were printed using non-dimensional rotation rates from $\overline{\omega}=0$ (zero nozzle rotation) to $\overline{\omega} = 4$ (high nozzle rotation). The print speed was fixed at 20 mm/s and the desired $\overline{\omega}$ values were produced by changing the nozzle rotation rate, summarized in Table 2. The samples printed without rotation ($\overline{\omega} = 0$) utilized a road-to-road spacing of 0.65 mm, while the rest of the samples utilized a road-to-road spacing of 0.872 mm. The wider spacing was necessary because the road width increases at higher $\overline{\omega}$ values for the same applied pressure. This may be a result of increased flow rate with rotation, or bulking of the material to accommodate reorientation of the fibers. All samples were printed onto glass substrates covered with PTFE-coated aluminum foil (Bytac, Saint-Gobain Performance Plastics, Worcester, MA) and were nominally 25 mm x 25 mm x 5 mm comprising five layers of unidirectional print paths. The samples were cured at atmospheric pressure and elevated temperature in two stages, first at 120 °C for 24 h and then at 200 °C for 2 h. Finally, 0.5 mm of material was machined away from the top of the printed samples to create a smooth surface for thermal conductivity measurements.

2.3. Characterization of thermal conductivity

Thermal conductivity measurements were performed using the transient planar source technique on a TPS 2500S instrument (ThermTest Inc, New Brunswick, Canada). The TPS 2500S was equipped with a module for testing anisotropic materials; a 40 mW power input was applied over a measurement duration of 10 s. The tests were set up by placing the coiled thermal sensor (covered in Kapton film) between two samples printed using the same print settings. The sample pieces were placed with their print directions parallel to one another and tested 5 times for each print configuration. Thermal conductivity measurements were obtained for through-thickness and average in-plane directions for each sample.

2.4. Microscopy and image analysis

Printed and cured samples were sectioned perpendicular to the axis of the printed roads using a low-speed diamond saw (TechCut 5, Allied High Tech Products, Inc., Rancho Dominguez, CA) and the cut surfaces were polished using a standard metallographic grinding and polishing wheel (M-Prep 5, Allied High Tech Products, Inc., Rancho Dominguez, CA). Optical micrographs were obtained with a VHX-5000 digital microscope (Keyence Corporation of America, Itasca, IL) and were

subsequently analyzed with Fiji (a variant of the ImageJ software [35]) to measure the shape and orientation of fiber profiles in the plane of examination, as well as the porosity. The micrograph images were first converted to 8-bit greyscale, then converted to black-and-white binary images using a threshold function to highlight only the cross-sections of the fibers. Next, the Analyze Particles function was used to identify the outlines of all features greater than 4 pixels in area (to eliminate measurement of erroneous small artifacts that were not fibers) and to fit an ellipse to each continuous outline. The major and minor axes, as well as the angle from horizontal to the major axis, were output in a list of comma-separated values for each fitted ellipse. These data were used to calculate the fiber orientation, as described in the following section. Between 3100 and 5700 ellipses were fit for each sample. To measure porosity, the original micrographs were converted to black-and-white using a different threshold value to highlight pores. The percent porosity was then approximated as the percentage of pixels contained in the pore regions.

3. Fiber orientation tensors

Assuming fibers are cylindrical with constant diameter along their length, the cross-section will appear as an ellipse when cut with a plane that is not perpendicular to the fiber axis Fig. 2(a-b)) [36-38]. The inverse cosine of the ratio of minor-to-major axis length for such an ellipse describes the angle, θ , of the fiber relative to the normal of the cut plane (Eq. (1) and Fig. 2(a)), while the angle, β , of the major axis of the ellipse with respect to a reference orientation, describes the angle of the fiber the relative to the plane of the baseplate and printed layer. From these two angles, the components of the unit vector describing the axis of the fiber can be calculated (Eqs. (2)–((4)). From the ensemble of orientations of individual fibers, fiber orientation tensors can be calculated to approximate the overall fiber orientation distribution function. This method was devised by Advani and Tucker [39], with various modifications and implementations by Bay and Tucker [36,40,41], Russell et al. [42], Vélez-García et al. [37], and Mlekusch [43], among many others. The unit vector describing orientation of a fiber axis, $\hat{p} = \langle p_1, p_2, p_3 \rangle$ p_3), is given by the following expressions:

$$\theta = \cos^{-1}\left(\frac{m}{M}\right) \tag{1}$$

$$p_1 = \cos\theta \tag{2}$$

$$p_2 = \sin\theta \cos\beta \tag{3}$$

$$p_3 = \sin\theta \sin\beta \tag{4}$$

Table 2Print parameters used for the thermal conductivity test samples.

Sample	Print speed (mm/s)	Nozzle diameter (mm)	In-plane road spacing (mm)	Nozzle rotation rate (rpm)	Dimensionless rotation rate $(\overline{\omega})$	Theoretical surface fiber angle, φ (degrees)
1	20	0.872	0.65	0	0	0
2	20	0.872	0.872	219	1	45
3	20	0.872	0.872	438	2	63
4	20	0.872	0.872	657	3	71
5	20	0.872	0.872	876	4	75

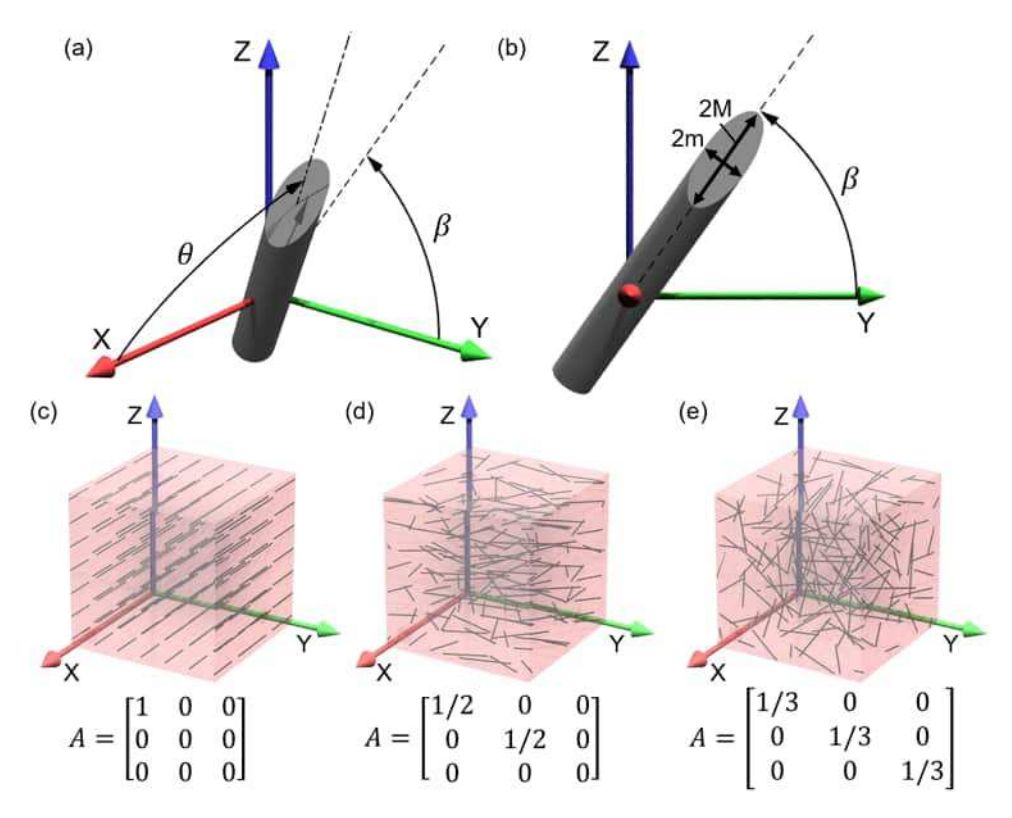


Fig. 2. Describing fiber orientation. (a) Two angles, θ and β , describe the orientation of a fiber relative to a coordinate system. (b) The cross section of a cylindrical fiber cut on an oblique plane forms an ellipse. The major and minor axes are used to calculate θ and the angle of the major axis corresponds to β . (c) Unidirectional fiber orientation and associated orientation tensor. (d) 2D random fiber orientation and associated orientation fiber orientation and associated orientation tensor.

Here, θ describes the angle measured from the x-axis to the fiber axis (the unit vector \hat{p}), and β describes the angle measured from the y-axis to the projection of the fiber axis onto the y-z plane (Fig. 2). We have chosen the y-z plane as the cut plane—since the printed samples were printed with unidirectional roads oriented in the x-direction—which leads to slightly different ordering of Eqs. (2)–(4) than was originally presented in Advani and Tucker, who chose the x-y plane as the cut plane. Finally, the unweighted components of the second-order orientation tensor, A, are obtained from the following summation [38,39]:

$$A_{ij} = \frac{1}{n} \sum_{k=1}^{n} (p_i p_j)_k \tag{5}$$

This is a 3×3 tensor that approximates the orientation distribution function of the fibers. For perfect unidirectional fiber orientation in the x-direction, $A_{11} = 1$ and all other values are zero (Fig. 2(c)). For 2D random fiber orientation within the x-y plane, $A_{11} = A_{22} = 1/2$ and all other terms are equal to zero (Fig. 2(d)). Finally, for 3D random fiber orientation, the second-order orientation tensor has equal values of 1/3 along the diagonal and all other terms are equal to zero (Fig. 2(e)). Here, it is important to note that a weighting function that depends on fiber length is typically used in the calculation of the components of the orientation tensor to account for the lower probability of a highly misoriented fiber crossing the section plane than a highly aligned fiber [36,37]. The weighting function serves to increase the relative weight of misoriented fibers in the averaging scheme. We have opted not to employ a weighting function here, since measurement of the fiber length distribution is beyond the scope and goals of the present work. As such, the fiber orientation values calculated here have a bias against misoriented fibers and the tensors will not be used to calculate any material properties, rather only used to qualitatively and conceptually rationalize thermal conductivity measurements.

The effectiveness of the printing process on imposing unidirectional fiber orientation depends on material formulation, constriction ratio, orifice diameter, and print speed, among other factors – see Hmeidat et al. [9,10], Kanarska et al. [44], and Trigg et al. [45], among others, for

detailed investigations of filler orientation in material extrusion AM.

4. Results

4.1. 3D printed specimens via RDIW

The printed samples are shown in Fig. 3(a). Increasing $\overline{\omega}$ resulted in rougher top surfaces from more exposed fibers and thicker roads. During printing, it was observed that the flow rate of the ink increased when rotation was used. This phenomenon is possibly a result of the additional shear being imposed on the shear-thinning ink, which lowered the effective viscosity and increased flow rate for the same applied pressure. Optical micrographs of the top surfaces reveal markedly different fiber texture when rotation is used, with the individual roads becoming more distinct with increasing rotation rate (Fig. 3(b)). For reference, the theoretical fiber orientation for a fiber at the top surface is overlayed in red on the micrographs in Fig. 3(b).

4.2. Thermal conductivity

For the sample printed without nozzle rotation, the through-thickness thermal conductivity was k=0.292 W/m.K, and the average in-plane thermal conductivity was k=0.456 W/m.K. As rotation rate increased from $\overline{\omega}=0$ to $\overline{\omega}=4$, the through-thickness thermal conductivity increased by 40% to k=0.409 W/m.K, while the average in-plane thermal conductivity first increased by 18% at $\overline{\omega}=1$, to k=0.539 W/m. K, then decreased to a minimum of k=0.420 W/m.K at $\overline{\omega}=3$ (Fig. 4). Thermal conductivity measurements and the associated anisotropy ratio, defined as the ratio of in-plane to through-thickness thermal conductivity, are summarized in Table 3.

4.3. Microstructure

Representative optical micrographs of the polished cross-sections of printed samples are shown in Fig. 5 for $\overline{\omega}=0$, 1, and 4 (Fig. 5(a-c)) along with the binarized versions of the same regions (Fig. 5(d-f)), and

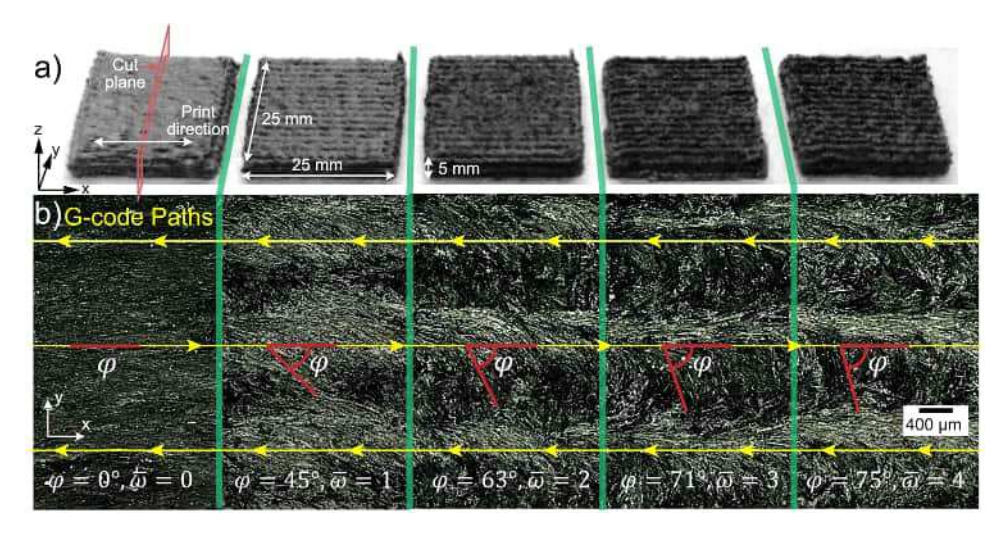


Fig. 3. (a) Photographs of $25 \times 25 \times 5$ mm samples printed by RDIW with varying nozzle rotation rates from $\overline{\omega} = 0$ (zero rotation) to $\overline{\omega} = 4$ (high rotation). (b) Optical micrographs showing the top surface for printed samples from $\overline{\omega} = 0$ to $\overline{\omega} = 4$; each macrograph is annotated with the theoretical surface fiber orientation relative to the road axis, based on the model suggested in [28]. The programmed printing paths in the g-code are indicated by the yellow arrows.

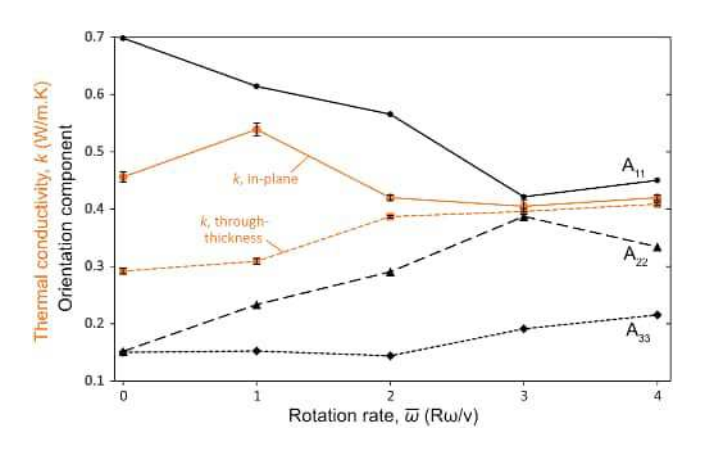


Fig. 4. Measured values of thermal conductivity in the through-thickness and in-plane directions and corresponding values of fiber orientation A_{11} , A_{22} , and A_{33} . The plot shows that as $\overline{\omega}$ increases, the measured thermal conductivity becomes more isotropic exemplified by convergence of the through-thickness and in-plane measurements.

detail views showing the fitted ellipses overlayed on the binarized micrographs (Fig. 5(g-i)). Fiber reorientation with rotation is immediately apparent, indicated by a transition from predominantly circular cross-sections for $\overline{\omega}=0$ (Fig. 5(a, d, g)) to increasing fractions of high aspect ratio ellipses for $\overline{\omega}=1$ (Fig. 5(b, e, h)) and $\overline{\omega}=3$ (Fig. 5(c, f, i)). It can be seen that the ellipse fitting is reasonably good, but there are some clear errors in fitting ellipses when fibers are touching and cannot be separated by the ImageJ analysis function. These errors are impractical to correct by hand across several images and may affect the accuracy of the orientation tensor components to some degree.

Some porosity can also be observed in the micrographs as large, round, black regions (Fig. 5(a-c)). Porosity increases from

approximately 5.0% for $\overline{\omega}=0$ to a maximum of 8.9% and 9.1% for $\overline{\omega}=1$ and $\overline{\omega}=2$, respectively, then reduces to approximately 7.6% and 5.8% for $\overline{\omega}=3$ and $\overline{\omega}=4$, respectively. Porosity values are summarized in Table 2.

The three diagonal components of the second-order fiber orientation tensor-calculated by applying the algorithm described in Section 4—are plotted in Fig. 4 along with the measured thermal conductivity values described in Section 5.2 and summarized in Table 2. As would be expected from the optical micrographs, the A₁₁ component is largest for the sample printed without rotation ($A_{11} = 0.698$), while the A_{22} and A_{33} components are nearly equal and close to zero ($A_{22} \approx A_{33} \approx 0.15$). As rotation is added and increased, A₁₁ steadily decreases while A₂₂ steadily increases. These components reach their respective minimum and maximum values at $\overline{w} = 3$, where $A_{11} = 0.422$ and $A_{22} = 0.387$. These values indicate that there is a significant reorientation of fibers into the y-direction (transverse to the print direction, in the layer plane), even though the x-direction (the print direction) is still the predominant fiber orientation. Interestingly, the A₃₃ component of the orientation tensor only increases mildly with rotation, from 0.150 to 0.215 at $\overline{\omega} = 4$. Despite the small absolute increase in value, this represents a 44% increase as a result of rotation and is likely the primary contributor to the observed increase in through-thickness thermal conductivity.

5. Discussion

This focused set of experiments shows that RDIW is a promising route to control the directionality of transport properties like thermal conductivity in 3D-printed composites. Based on the simple kinematic model first proposed by Raney et al. [28], one would expect the transverse components of fiber orientation, A_{22} and A_{33} , to be equivalent. However, that was not observed here, and instead the in-plane transverse orientation component (A_{22}) increased with rotation much more than the through-thickness transverse component (A_{33}). This is likely because the ideal kinematic model does not account for any of the

Table 3Thermal conductivity and fiber orientation measurements.

	k , through-thickness $(W/m\cdot K)$	k , in-plane $(W/m\cdot K)$	Thermal anisotropy ratio	Porosity (%)	A_{11}	A_{22}	A ₃₃
0	0.292 ± 0.005	0.456 ± 0.009	1.562	5.0	0.698	0.152	0.150
1	0.309 ± 0.005	0.539 ± 0.011	1.744	8.94	0.614	0.233	0.152
2	0.387 ± 0.002	0.420 ± 0.005	1.085	9.14	0.565	0.291	0.144
3	0.396 ± 0.005	0.405 ± 0.010	1.023	7.62	0.422	0.387	0.191
4	0.409 ± 0.003	0.420 ± 0.005	1.027	5.77	0.450	0.334	0.215

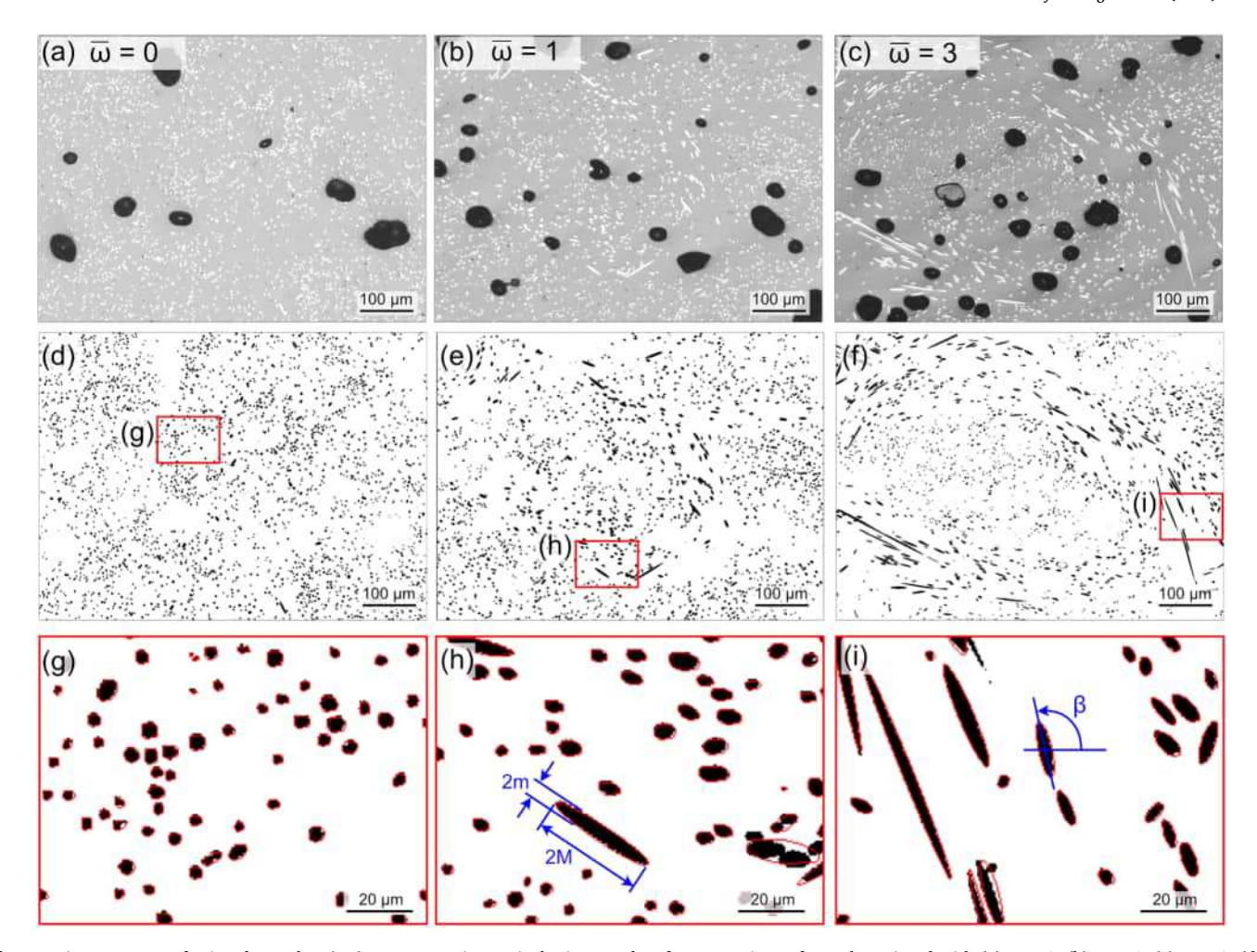


Fig. 5. Microstructure of printed samples. (a-c) Representative optical micrographs of cross-sections of samples printed with (a) $\overline{\omega}=0$, (b) $\overline{\omega}=1$, (c) $\overline{\omega}=3$. (d-f) Binarized micrographs of the same regions to highlight fiber cross-sections for (d) $\overline{\omega}=0$, (e) $\overline{\omega}=1$, (f) $\overline{\omega}=3$. (g-i) Detail views of select regions of the binarized micrographs overlayed with the fitted ellipses used to calculate the fiber orientation tensors.

deformation that the road experiences after it exits the nozzle. Two additional deformation modes are active that could reduce or undo some of the fiber reorientation in the through-thickness direction: the extruded road is compressed between the substrate and the nozzle [46], leading to a squeeze flow-like scenario that would accentuate in-plane fiber orientation; and the deposited material causes shear deformation in the adjacent roads [45] that could undo some of the through-thickness reorientation on one side of each road.

It is also important to note potential sources of error in the fiber orientation analysis that affect the accuracy of the components of the fiber orientation tensor in describing the true fiber orientation distribution function. First, orientation tensors are approximations of the probability distribution function for fiber orientation, with the second order tensor being a coarser approximation than higher order tensors [39]. Advani and Tucker also showed that the second order tensor is less accurate at describing highly aligned fibers than it is at describing more random fiber orientation distributions [39]. Additionally, the method for calculating fiber orientation from optical micrographs is imperfect, being sensitive to choices of threshold parameters, being unable to separately analyze fibers that are touching, and being sensitive to choice of a weighting function for misoriented fibers [36,37], among other factors. An example of clumped fibers being misinterpreted is highlighted in Fig. 5(g-i). For highly aligned fibers, fiber clumping will lead to some highly oriented fibers being erroneously categorized as misoriented relative to the alignment direction—for example, two or three aligned fibers that are touching will be analyzed as one ellipse with an

apparent misorientation. Conversely, clumps of highly misoriented fibers tend to be fit with ellipses having lower aspect ratio-and therefore lower apparent misorientation-than the individual fibers comprising the clump (Fig. 5(i)). In this sense, the components of the orientation tensors calculated here would tend to be more conservative than the physical case. In conducting these analyses, the authors did not observe drastic changes to the calculated orientation tensors as a result of small changes to the choice of thresholding parameters. However, to be clear, the intent of the orientation calculations conducted here was not to definitively establish universal fiber orientation relationships, but simply to provide approximate quantitative characterization of microstructure to rationalize the thermal conductivity measurements and motivate further in-depth research in this area. Discussion on maximizing accuracy of optical fiber orientation measurements can be found in Velez-Garcia et al. [37]. Readers are also directed to Bay and Tucker [36] for detailed discussion of weighting functions and error estimates in calculating fiber orientation tensors from optical micrographs, as well as Jack and Smith [47] for a detailed treatment of the statistical aspects of fiber orientation and the associated expectation and variance values for elastic properties calculated from orientation tensors.

In order to maximize through-thickness or transverse in-plane thermal conductivity (or any other properties that derive from fiber orientation), a detailed study of the relationships between rotation, fiber orientation, porosity, and print parameters (e.g., gap height, road overlap, print speed, and nozzle diameter) is needed. Additional factors may include how effective the carrier fluid is in rapidly reorienting

fibers (i.e., the relationship between carrier fluid viscosity and fiber orientation), and the effect of fiber length relative to the nozzle outlet diameter. Higher print speed and smaller nozzle diameter have been shown to impart greater fiber orientation in printed composites using conventional DIW, but it is presently unclear how these parameters affect fiber orientation in RDIW. Longer fibers generally lead to better mechanical and transport properties, but fibers that are a significant fraction of, or longer than, the nozzle diameter or layer thickness, would be geometrically constrained from reorienting as much as shorter, smaller fibers, like whiskers or nanotubes, for example. Such studies are ongoing and will be key to realizing full spatial control of mechanical and transport properties in 3D-printed composites.

6. Conclusions

This work shows for the first time that the through-thickness thermal conductivity of 3D-printed composites can be significantly increased by rotating the deposition nozzle using RDIW. For the material system studied here - short carbon fiber-reinforced epoxy - the throughthickness thermal conductivity increased by 40% at the highest rotation rate investigated. Second-order fiber orientation tensors calculated from optical micrographs of polished cross-sections — also calculated for the first time for a composite printed using RDIW — provided quantitative information about how fiber orientation changes with nozzle rotation rate. Experiments showed that fibers do not reorient symmetrically about the road axis in bulk printed composites, as the kinematic model put forth by Raney et al. [28] assumed, leading to distinct differences between the in-plane transverse (A22) and through-thickness transverse fiber orientations (A₃₃). These differences are attributed to the additional deformation that the extruded road experiences as a result of squeeze flow between the nozzle and substrate, and the shear that occurs between adjacent roads within the same printed layer. A more detailed understanding of the relationships between gap height, road spacing, ink properties, nozzle rotation rate, and fiber orientation is greatly needed and would allow further optimization and utilization of RDIW in myriad applications like heat exchangers, high speed flight parts, tooling, and wear components.

Declaration of Competing Interest

The authors declare that they have no known competing financial interests or personal relationships that could have appeared to influence the work reported in this paper.

Data availability

Data will be made available on request.

Acknowledgments

The authors gratefully acknowledge financial support from Honeywell Federal Manufacturing & Technologies through contract DE-NA0002839. NSH and BGC would like to acknowledge partial support from the National Science Foundation under Grant No. 1825815, and the Tennessee Higher Education Commission (THEC) Center for Materials Processing (CMP) at the University of Tennessee, Knoxville. Professors Doug Aaron and Matthew Mench are also gratefully acknowledged for providing access and assistance with the thermal conductivity measurements.

References

[1] T.D. Ngo, A. Kashani, G. Imbalzano, K.T. Nguyen, D. Hui, Additive manufacturing (3D printing): a review of materials, methods, applications and challenges, Compos. Part B Eng. 143 (2018) 172–196.

- [2] B. Brenken, E. Barocio, A. Favaloro, V. Kunc, R.B. Pipes, Fused filament fabrication of fiber-reinforced polymers: a review, Addit. Manuf. 21 (2018) 1–16.
- [3] B.G. Compton, J.A. Lewis, 3D-printing of lightweight cellular composites, Adv. Mater. 26 (34) (2014) 5930–5935, https://doi.org/10.1002/adma.201401804.
- [4] F. Ning, W. Cong, J. Qiu, J. Wei, S. Wang, Additive manufacturing of carbon fiber reinforced thermoplastic composites using fused deposition modeling, Compos. Part B Eng. 80 (2015) 369–378.
- [5] H.L. Tekinalp, V. Kunc, G.M. Velez-Garcia, C.E. Duty, L.J. Love, A.K. Naskar, C. A. Blue, S. Ozcan, Highly oriented carbon fiber-polymer composites via additive manufacturing, Compos. Sci. Technol. 105 (2014) 144–150, https://doi.org/10.1016/j.compscitech.2014.10.009.
- [6] B.G. Compton, J.K. Wilt, J.W. Kemp, N.S. Hmeidat, S.R. Maness, M. Edmond, S. Wilcenski, J. Taylor, Mechanical and thermal properties of 3D-printed epoxy composites reinforced with boron nitride nanobarbs, MRS Commun. 11 (2021) 100–105.
- [7] G. Postiglione, G. Natale, G. Griffini, M. Levi, S. Turri, Conductive 3D microstructures by direct 3D printing of polymer/carbon nanotube nanocomposites via liquid deposition modeling, Compos. Part A Appl. Sci. Manuf. 76 (2015) 110–114.
- [8] N.S. Hmeidat, J.W. Kemp, B.G. Compton, High-strength epoxy nanocomposites for 3D printing, Compos. Sci. Technol. 160 (2018) 9–20, https://doi.org/10.1016/j. compscitech.2018.03.008.
- [9] N.S. Hmeidat, D.S. Elkins, H.R. Peter, V. Kumar, B.G. Compton, Processing and mechanical characterization of short carbon fiber-reinforced epoxy composites for material extrusion additive manufacturing, Compos. Part B Eng. 223 (2021), 109122, https://doi.org/10.1016/j.compositesb.2021.109122.
- [10] N.S. Hmeidat, R.C. Pack, S.J. Talley, R.B. Moore, B.G. Compton, Mechanical anisotropy in polymer composites produced by material extrusion additive manufacturing, Addit. Manuf. 34 (2020), 101385, https://doi.org/10.1016/j. addma.2020.101385.
- [11] D.E. Yunus, W. Shi, S. Sohrabi, Y. Liu, Shear induced alignment of short nanofibers in 3D printed polymer composites, Nanotechnology 27 (49) (2016), 495302.
- [12] B. Brown, N.S. Hmeidat, X. Jia, J. Wilt, M. Roberts, B.G. Compton, N. Vermaak, Experimental investigations of the effectiveness of simultaneous topology/ orientation optimization via SOMP and principal stress directions, Mater. Des. 217 (2022), 110647.
- [13] H. Prüß, T. Vietor, Design for fiber-reinforced additive manufacturing, J. Mech. Des. 137 (11) (2015), 111409.
- [14] T. Shafighfard, T.A. Cender, E. Demir, Additive manufacturing of compliance optimized variable stiffness composites through short fiber alignment along curvilinear paths, Addit. Manuf. 37 (2021), 101728.
- [15] T. Suzuki, S. Fukushige, M. Tsunori, Load path visualization and fiber trajectory optimization for additive manufacturing of composites, Addit. Manuf. 31 (2020), 100942.
- [16] E. Huttunen, M.T. Nykänen, J. Alexandersen, Material extrusion additive manufacturing and experimental testing of topology-optimised passive heat sinks using a thermally-conductive plastic filament. Addit. Manuf. 59 (2022), 103123.
- [17] Y. Jia, H. He, Y. Geng, B. Huang, X. Peng, High through-plane thermal conductivity of polymer based product with vertical alignment of graphite flakes achieved via 3D printing, Compos. Sci. Technol. 145 (2017) 55–61.
- [18] K. Li, T. Smith, W. Asher, A. Flores-Betancourt, A.A. Trofimov, H. Wang, M. Zhang, L. Kearney, E. Lara-Curzio, S. Ozcan, Additively manufactured polymer composites for heat exchanger applications: evaluation of critical thermophysical properties, J. Mater. Sci. 58 (2023) 11585–11596.
- [19] L. Lu, Z. Zhang, J. Xu, Y. Pan, 3D-printed polymer composites with acoustically assembled multidimensional filler networks for accelerated heat dissipation, Compos. Part B Eng. 174 (2019), 106991.
- [20] S.L. Schleifer, O. Regev, Additive manufacturing of anisotropic graphene-based composites for thermal management applications, Addit. Manufact. 70 (2023), 103567.
- [21] Y. Kim, H. Yuk, R. Zhao, S.A. Chester, X. Zhao, Printing ferromagnetic domains for untethered fast-transforming soft materials, Nature 558 (7709) (2018) 274–279.
- [22] M. Roy, P. Tran, T. Dickens, A. Schrand, Composite reinforcement architectures: a review of field-assisted additive manufacturing for polymers, J. Compos. Sci. 4 (1) (2019) 1.
- [23] L.R. Holmes Jr, J.C. Riddick, Research summary of an additive manufacturing technology for the fabrication of 3D composites with tailored internal structure, JOM 66 (2) (2014) 270–274.
- [24] Y. Yang, X. Li, M. Chu, H. Sun, J. Jin, K. Yu, Q. Wang, Q. Zhou, Y. Chen, Electrically assisted 3D printing of nacre-inspired structures with self-sensing capability, Sci. Adv. 5 (4) (2019) eaau9490.
- [25] K. Johnson, D. Melchert, D.S. Gianola, M. Begley, T.R. Ray, Recent progress in acoustic field-assisted 3D-printing of functional composite materials, MRS Adv. 6 (2021) 636–643.
- [26] M.S. Scholz, B. Drinkwater, R. Trask, Ultrasonic assembly of anisotropic short fibre reinforced composites, Ultrasonics 54 (4) (2014) 1015–1019.
- [27] D.E. Yunus, S. Sohrabi, R. He, W. Shi, Y. Liu, Acoustic patterning for 3D embedded electrically conductive wire in stereolithography, J. Micromech. Microeng. 27 (4) (2017), 045016.
- [28] J.R. Raney, B.G. Compton, J. Mueller, T.J. Ober, K. Shea, J.A. Lewis, Rotational 3D printing of damage-tolerant composites with programmable mechanics, Proc. Natl. Acad. Sci. 115 (6) (2018) 1198–1203, https://doi.org/10.1073/pnas.1715157115.
- [29] C. Mo, H. Long, J.R. Raney, Tough, aorta-inspired soft composites, Proc. Natl. Acad. Sci. 119 (28) (2022), e2123497119.

- [30] N.M. Larson, J. Mueller, A. Chortos, Z.S. Davidson, D.R. Clarke, J.A. Lewis, Rotational multimaterial printing of filaments with subvoxel control, Nature 613 (7945) (2023) 682–688.
- [31] M. Spoerk, C. Savandaiah, F. Arbeiter, G. Traxler, L. Cardon, C. Holzer, J. Sapkota, Anisotropic properties of oriented short carbon fibre filled polypropylene parts fabricated by extrusion-based additive manufacturing, Compos. Part A Appl. Sci. Manuf. 113 (2018) 95–104.
- [32] H. Pierson, E. Celik, A. Abbott, H. De Jarnette, L.S. Gutierrez, K. Johnson, H. Koerner, J. Baur, Mechanical properties of printed epoxy-carbon fiber composites, Exp. Mech. (2019) 1–15.
- [33] Hexcel. https://www.rockwestcomposites.com/media/wysiwyg/AS4.pdf 2010.
- [34] Scilab. http://www.scilab.org. 1990.
- [35] J. Schindelin, I. Arganda-Carreras, E. Frise, V. Kaynig, M. Longair, T. Pietzsch, S. Preibisch, C. Rueden, S. Saalfeld, B. Schmid, Fiji: an open-source platform for biological-image analysis, Nat. Methods 9 (7) (2012) 676–682.
- [36] R.S. Bay, C.L. Tucker III, Stereological measurement and error estimates for threedimensional fiber orientation, Polym. Eng. Sci. 32 (4) (1992) 240–253.
- [37] G.M. Vélez-García, P. Wapperom, D.G. Baird, A.O. Aning, V. Kunc, Unambiguous orientation in short fiber composites over small sampling area in a center-gated disk, Compos. Part A Appl. Sci. Manuf. 43 (1) (2012) 104–113.
- [38] J. Weissenböck, M. Arikan, D. Salaberger, J. Kastner, J. De Beenhouwer, J. Sijbers, S. Rauchenzauner, T. Raab-Wernig, E. Gröller, C. Heinzl, Comparative visualization of orientation tensors in fiber-reinforced polymers, in: Proceedings of the 8th Conference on Industrial Computed Tomography (iCT 2018), Wels, Austria, 2018.

- [39] S.G. Advani, C.L. Tucker III, The use of tensors to describe and predict fiber orientation in short fiber composites, J. Rheol. 31 (8) (1987) 751–784.
- [40] R.S. Bay, C.L. Tucker III, Fiber orientation in simple injection moldings. Part II: experimental results, Polym. Compos. 13 (4) (1992) 332–341.
- [41] R.S. Bay, C.L. Tucker III, Fiber orientation in simple injection moldings. Part I: theory and numerical methods, Polym. Compos. 13 (4) (1992) 317–331.
- [42] T. Russell, B. Heller, D.A. Jack, D.E. Smith, Prediction of the fiber orientation state and the resulting structural and thermal properties of fiber reinforced additive manufactured composites fabricated using the big area additive manufacturing process, J. Compos. Sci. 2 (2) (2018) 26.
- [43] B. Mlekusch, Fibre orientation in short-fibre-reinforced thermoplastics II. Quantitative measurements by image analysis, Compos. Sci. Technol. 59 (4) (1999) 547–560
- [44] Y. Kanarska, E. Duoss, J. Lewicki, J. Rodriguez, A. Wu, Fiber motion in highly confined flows of carbon fiber and non-Newtonian polymer, J Non Newton. Fluid Mech. 265 (2019) 41–52.
- [45] E.B. Trigg, N.S. Hmeidat, L.M. Smieska, A.R. Woll, B.G. Compton, H. Koerner, Revealing filler morphology in 3D-printed thermoset nanocomposites by scanning microbeam X-ray scattering, Addit. Manuf. 37 (2021), 101729.
- [46] C. Duty, C. Ajinjeru, V. Kishore, B. Compton, N. Hmeidat, X. Chen, P. Liu, A. A. Hassen, J. Lindahl, V. Kunc, What makes a material printable? A viscoelastic model for extrusion-based 3D printing of polymers, J. Manuf. Process. 35 (2018) 526–537, https://doi.org/10.1016/j.jmapro.2018.08.008.
- [47] D.A. Jack, D.E. Smith, Elastic properties of short-fiber polymer composites, derivation and demonstration of analytical forms for expectation and variance from orientation tensors, J. Compos. Mater. 42 (3) (2008) 277–308.